Memoria Trabajo de Fin de Grado

3D FS-Laser nanostructuring of YAG crystals: Laboratory Experiments and a numerical design of optical waveguides.

Departamento de Física

Facultad de Ciencias.

Grado en Física.

Autora: Inés Meili Díaz García

Tutor: Dr. Airán Ródenas Seguí

4 de julio de 2022.

Contents

Abstract.

In this final degree project, a study of the fabrication and implementation of 3D photonic structures at nanometric and micrometric scales was carried out. In particular, the study was based around the concept of photonic crystals and microstructured optical waveguides, as technology goal. It starts defining the theoretical framework in which these structures of interest are based on and their interactions with external factors, such as light. To do this, it was necessary to go to theoretical concepts of periodic structures which define these photonic objects and a review of the Electromagnetism and Optics definitions and equations has been done. Furthermore, the experimental technique for fabricating a periodic pattern with hollow nanopores in the material by means of femtosecond-pulse laser irradiation, has been studied. During this project, the material which was used was YAG crystal (yttrium aluminium garnet). To achieve this, it was necessary the use of different technological devices such as a femtosecond-pulse laser, a pulse-picker, a computer controlled 3D nanopositioning system, an optical microscope, an electron microscope, optical polishing machine, wet-chemical etching infrastructure, and also numerical simulation tools (commercial BandSOLVE software).

Once the nanolithography technique used for obtaining nanopores was studied, the elaboration of experiments was carried out, also with the assistance of PhD student, Franzette Paz Buclatin. The goal was to study the characteristics of this lithography technique, which is based on a technique discovered by the supervisor Dr. Ródenas. Therefore, an analysis was developed in order to study the dependence between the pore length, and also its sub-micron cross-sectional shape and size, as a function of some fabrication parameters such as: pulse repetition rate of the laser, pulse energy, or laser writing speed. To achieve this objective, the use of the image processing software ImageJ was needed. For this last task, it was necessary additional support from SEGAI facilities with the purpose of using the scanning electron microscope (SEM).

Also, through this project, the BandSOLVE RSOFT software was used. The implementation of this software allowed to put into practice the theoretical knowledge about periodic structures in an easy to use numerical simulation framework. Doing this, it was possible to make an optimization process of an hexagonal lattice with the purpose of obtaining the most suitable characteristics for designing and studying a photonic waveguide, from the UV to the IR range in the electromagnetic spectrum. The EM range of interest was limited to the transparency range of YAG, from around 250 nm (UV) to 5000 nm (mid-IR), for which the dispersion of the index of refraction of the crystal was always taken into account.

Resumen.

En este trabajo de fin de grado se ha realizado un estudio de la fabricación y aplicación de estructuras fotónicas en 3D en las escalas nanométrica y micrométrica. Concretamente, el estudio se basó en el concepto de cristales fotónicos y en guías de onda ópticas microestructuradas como objetivo tecnológico. El proyecto comienza definiendo el marco teórico en el que están basadas estas estructuras de interés y sus interacciones con factores externos, como puede ser la luz. Para ello, se ha recurrido a conceptos teóricos de estructuras periódicas que definen estos objetos fotónicos y se ha realizado un repaso de definiciones y ecuaciones relacionadas tanto con el ámbito del Electromagnetismo como con el de la Óptica. Además, se ha estudiado en detalle la técnica experimental desarrollada para la fabricación de un patrón periódico con nanoporos huecos en el material mediante la irradiación láser de pulsos de femtosegundos. Durante este trabajo, el material utilizado fue el cristal de YAG. ("yttrium aluminium garnet"). Para lograr esto fue necesario el uso de diversos dispositivos tecnológicos como un láser de femtosegundos, un "pulse-picker", un sistema de nanoposicionamento 3D controlado por ordenador, un microscopio óptico, un microscopio de electrones, una máquina de pulido óptico, infraestructuras de grabado químico húmedo y además, herramientas de simulación numéricas (software comercial del BandSOLVE).

Una vez estudiada la técnica de nanolitografía para la obtención de nanoporos, se procedió a la elaboración de experimentos con la ayuda de la estudiante de tesis doctoral PhD, Franzette Paz Buclatin. El objetivo era llevar a cabo un estudio sobre las características de esta técnica de litografía basada en una técnica descubierta por el tutor Dr. Ródenas. Por tanto, se realizó un análisis para estudiar la dependencia de la longitud de poros y su forma y tamaño transversal submicrométricos en función de diferentes parámetros del proceso de fabricación como: el ritmo de repetición del láser, energía de pulso o velocidad de escritura del láser. Para alcanzar este objetivo se hizo uso del programa de procesamiento de imágenes ImageJ. En este último caso fue necesario recurrir a servicios adicionales como el SEGAI para la utilización del microscopio electrónico de barrido.

Además, durante este proyecto, también se utilizó el software BandSOLVE RSOFT. La aplicación de este software permitió poner en práctica los conocimientos teóricos sobre estructuras periódicas en un sencillo marco de simulación numérica. De esta manera, fue posible realizar una optimización de una red hexagonal con el objetivo de obtener las características más adecuadas para el diseño y estudio de una guía de ondas fotónica, desde el rango del UV hasta el IR en el espectro electromagnético. El rango electromagnético de interés fue limitado al rango de transparencia del YAG, desde aproximadamente 250 nm (UV) hasta 5000 nm (mid-IR), para lo cual se tuvo siempre en cuenta la dispersión del índice de refracción del cristal.

Chapter 1

Introduction.

En este apartado se realiza una breve introducción al concepto de dispositivo fotónico y a sus aplicaciones. Además, se hace una pequeña descripción de los motivos que llevaron al desarrollo de la técnica de trabajo y su respectiva propuesta a la hora de formalizarlo como técnica de obtención de los objetos de estudio. Finalmente, se mencionan algunas de las aplicaciones de estos dispositivos como los cristales fotónicos y guías de onda fotónica.

Following the definition adopted by Karlsruhe University, "photonics is the science and technology of generating, controlling and detecting photons, particularly in the visible and near infra-red light spectrum" [1].

There are different devices based on photonic technology, a remarkable example would be photonic crystals. The main difference with an ordinary crystal is that photonic crystals have a lattice constant which is comparable in magnitude to the wavelength of the light and, when they interact with it, present a photonic band structure [1].

To obtain this kind of structures, it is necessary to modify certain materials at a 3D level, in this case, optical crystals. Despite the fact that 2D nanolithography was completely developed, extending from 2D to 3D was challenging and motivated researchers to look for the best procedures and materials in order to achieve this objective. A first approach was presented several decades ago using a resin photo-polymerization process [2]. However, the material used in this method was not capable of interacting with other photonic materials so, it was considered unfeasible.

As an alternative to these failed attempts, Dr. Ródenas et al. presented a new type of methodology. This technique involves the role of a laser to make written tracks in the crystal by photo-modifications. After that, a chemical etching using an acid composition is needed in order to obtain hollow pores (air pores) in a certain spatial disposition and consequently, a photonic crystal [3].

Another photonic device studied during this project was a Microstructured Optical Waveguide (MOW). In particular, these waveguides are designed within a crystal as a periodic array of air hollow sub-micron straight pores, which can be obtained using the technique detailed in the previous paragraph. The main characteristic in this type of structures is that light propagates because of the existence of a refractive index difference caused by a defect in the nanopore lattice which, in this case, is the absence of an air pore in the center region so that a volume of dielectric is created through which light can propagate. Although it is not necessary, we will see that the particular waveguide that it is studied in this project exhibits a bandgap at a certain frequency which it is believed it could improve optical losses, although that

needs from further research beyond the scope of this final degree project.

Chapter 2

Objectives.

En este apartado se detallará el principal objetivo de este trabajo y las razones que motivaron al proceso de investigación. El propósito primordial fue el estudio y entendimiento de la técnica para realizar estructuración a escala nanométrica en cristales. De este último se pudieron derivar otros objetivos tanto teóricos como prácticos.

The main objective of this project was the study of the 3DLW ("3D Laser Writing") and chemical etching technique and its implementation for fabricating photonic devices. In particular, the study of photonic crystals was developed. Within this main objective and apart from it, there were other goals that were purposed.

- Studying photonic devices and their applications in the technological field.
- Acquiring knowledge about periodic structures and other concepts derived from this topic, such as band diagrams or bandgaps.
- Following a PhD student scientific routine with the purpose of learning the work dynamic in a laboratory.
- Understanding the use of different laboratory instruments and microscopes.
- Learning the use of an image processing software and a simulation software for our purpose.
- Making interpretations of the simulated results in order to implement them in a laboratory work.

Chapter 3

Methodology.

En este apartado se desarrollarán de manera breve las definiciones y conceptos teóricos en los que se basan algunos de los experimentos o simulaciones. Además, se detallarán los procesos y recursos utilizados para la obtención de las muestras y su posterior medición de los parámetros de interés.

3.1 Theory of band structures and bandgaps.

A periodic structure can be found in any device in our day to day. There are lots of tools that, despite the fact of not seeing it at first sight, contain periodic configurations. For example: diffraction gratings, antennas, waveguides... Also, they show up in more complex apparatus such as slow wave devices or metamaterials [1].

A formal definition of a periodic structure would be a configuration whose elements obey some symmetry statements such as pure translations, pure reflections... It has to be kept in mind that, during this project, periodic structures that we will be talking about belong to bigger scales than the atomic one.

Once we have introduced the concept of periodic structure, it is convenient to expound the categories in which they can be classified. In 3D there are 14 Bravais Lattices (looking at the disposition of the elements) and within it, there are 7 Crystal Systems (looking at the outline of the unit cell, concept that will be defined soon). This classification is explained in Subfigure (3.1a). However, in 2D there are only 5 Bravais Lattices. See Subfigure (3.1b).

Examining these structures, one can find that the hexagonal lattice possess the highest packing density in 2D. This will be important because a 2D hexagonal lattice will be studied during this project.

[1] Metamaterial: periodic structures with a lattice constant smaller than light wavelength and can present negative refractive index. Also they produce artificial permittivity and permeability [1],[4].

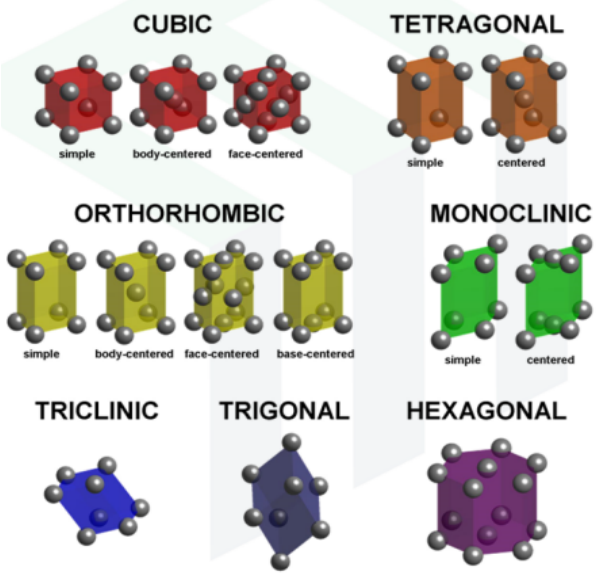

(a) 14 Bravais Lattices and 7 Crystal Systems in 3D.

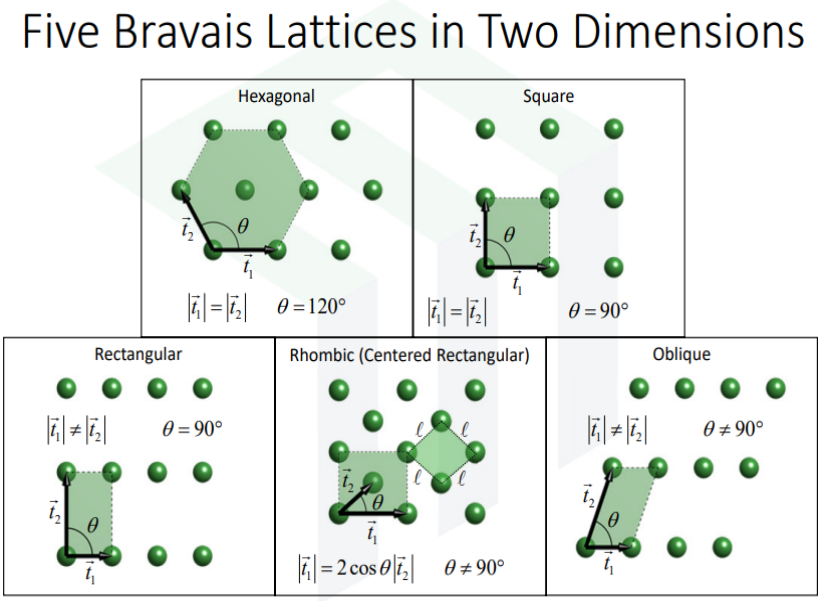

(b) 5 Bravais Lattices in 2D.

Figure 3.1: Classification of periodic structures in 3D and 2D. Adapted from Rumpf, R.C (May 2020). Introduction to Periodic Structures in Electromagnetics. [PowerPoint slides]. Retrieve from `https://empossible.net/academics/emp6303/`.

Now, it is time to define some of the elements that characterize a periodic lattice, e.g., unit cell, vectors...

A unit cell is the tiniest structure that can be repeated in order to recreate the whole periodic lattice. At the same time, a unit cell can be classified as a primitive unit cell or a conventional unit cell. The first one contains only one lattice point within it and has the smallest possible volume and the latter can have more than one [6].

Now we are going to describe vectors. There are mainly two types depending on

whether they describe the 7 Crystal Systems (axis vectors) or the 14 Bravais Lattices (translation vectors). Both types are composed by three vectors. Also, it is convenient to know the concept of primitive vectors. These are those vectors which, from a certain point, point to others immediately next to it. Therefore, they are the smallest vectors that can characterize a unit cell. In addition, primitive translation vectors define the direct lattice as it is indicated in Figure (3.2). This is the real lattice, the one that can be touched.

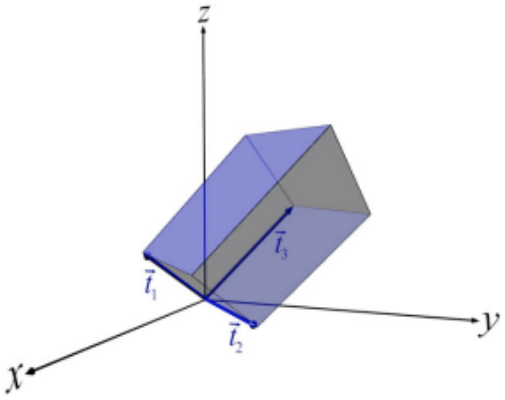

Figure 3.2: Direct lattice and primitive translation vectors. Adapted from Rumpf,R.C (May 2020). Lattice Vectors.[PowerPoint slides]. Retrieve from `https://empossible.net/academics/emp6303/`

.

Once we have defined the direct lattice, it is time to define the reciprocal lattice. One can take two of the primitive translation vectors (as we said they were three, e.g., $\vec{t_1}$ and $\vec{t_2}$) and constitute a plane. This plane, as it is defined in a periodic structure, is repeated over a period labeled as Λ_3. In the perpendicular direction to these planes it is determined a reciprocal lattice vector, $\vec{T_3}$. Figure (3.3) shows a visual idea of this method. This new vector is described by Equation (3.1).

$$\vec{T_3} = \frac{2\pi}{\Lambda_3} \tag{3.1}$$

If we repeated the same procedure for the rest of vector combinations, we would obtain the remainder reciprocal lattice vectors. Once these vectors are defined, we can define the reciprocal lattice in an analogous way as we did with the direct lattice. This reciprocal lattice is very important because, despite the fact of not being touchable or real, it describes the symmetry of the direct lattice and both obey the same physical laws.

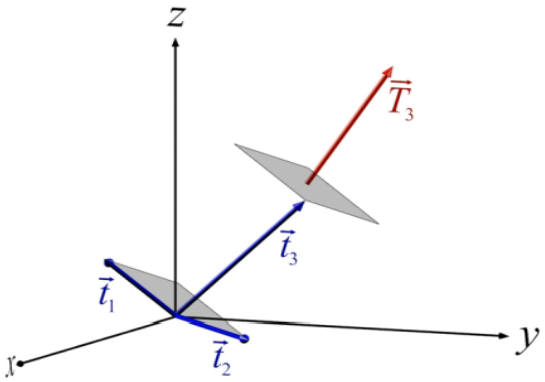

Figure 3.3: Graphical method of obtaining a reciprocal lattice vector. Adapted from Rumpf,R.C (May 2020). Lattice Vectors.[PowerPoint slides]. Retrieve from `https://empossible.net/academics/emp6303/`

.

We said before that a primitive unit cell can be defined in a direct lattice. To achieve this, the Wigner-Seitz cell method can be used and the resulting primitive unit cell is known as the Wigner-Seitz primitive unit cell. As both lattices (direct and reciprocal) must obey the same laws, the equivalent in the reciprocal lattice would be the Brillouin Zone. Taking advantage of some additional symmetry that exists at the Brillouin Zone, it is possible to define a smaller volume inside it that also characterizes the periodicity of the lattice and it is known as the Irreducible Brillouin Zone.

At this point, where the concept of periodic lattice has been explained, it is time to describe the behavior of an electromagnetic wave passing through these structures.

When an electromagnetic wave with a wave vector $\vec{k}$ passes through a periodic structure, it can be described with Equation (3.2) [7].

$$\vec{E}(\vec{r}) = \vec{A}(\vec{r}) \cdot e^{j\vec{\beta}\cdot\vec{r}} \tag{3.2}$$

Where:

- $\vec{A}(\vec{r})$: envelope function.
- $e^{j\vec{\beta}\cdot\vec{r}}$: plane wave function.
- $\vec{\beta}$: Bloch wave vector $|\vec{\beta}| = \frac{2\pi}{\lambda}$.

Then, if Ecuation (3.3) (compact way of writing Maxwell equations) is solved, considering the characteristics of the lattice, the results obtained would be the eigenvalues ($k_{0,i}^2$) and eigenvectors ($\vec{H}_i$) ($i = 1, 2, 3, ..., \infty$). The first one give us information about the frequency that the wave acquires when it passes through the material and the latter shows the magnetic field represented as form of mode profiles. The results of this equation come out in pairs. In other words, for every eigenvalue, there is an eigenvector.

$$\nabla \times \frac{1}{\varepsilon_r} \nabla \times \vec{H} = k_0^2 \vec{H} \tag{3.3}$$

The idea would be to solve Equation (3.3) for each point at the Irreducible Brillouin Zone but this would take a lot of calculation time. So, an alternative is to calculate these eigenvalues and eigenvectors just in the perimeter of the Irreducible Brillouin Zone. A plot of the eigenvalues in a finite number of points (symmetry points) along this perimeter would be a band diagram [7]. We can see an example of what we would obtain in Figure (3.4).

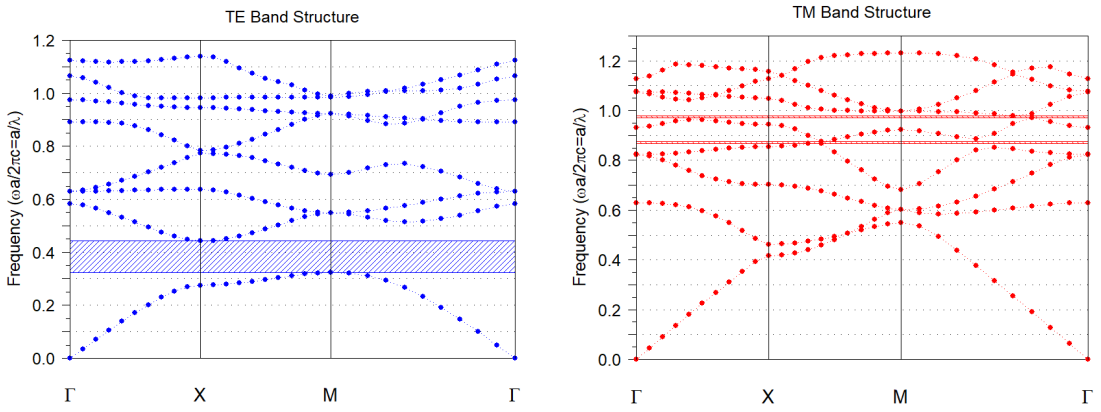

(a) TE band diagram.

(b) TM band diagram.

Figure 3.4: Band diagrams of a 2D rectangular array. The values that $\vec{\beta}$ takes are the symmetry points represented in x-axis and normalized frequency is represented in y-axis.

The dotted lines are the bands and the absence of bands constitutes a bandgap. Following these definitions, a complete bandgap is defined as the non-existence of bands in the whole range of Bloch wave vectors. These are the shaded regions. When a bandgap exists, a zero transmission effect and enhanced reflection occur. Also, other parameters as phase velocity or group velocity can be determined using these diagrams.

If we had calculated the eigenvalues and eigenvectors within the whole Brillouin Zone, we would have obtained the complete band diagram. See Figure (3.5).

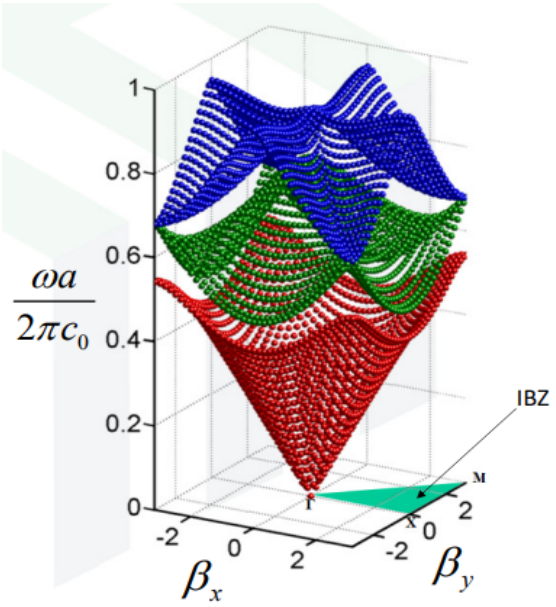

Figure 3.5: Completed band diagram.Adapted from Rumpf,R.C (May 2020). Electromagnetic Waves in Periodic Structures.[PowerPoint slides]. Retrieve from `https://empossible.net/academics/emp6303/`

3.2 3D Laser Writing (3DLW) Nanolithography and Chemical Etching.

The technique that provides us suitable materials for the study is the 3D femtosecond laser nanolithography, followed by a chemical etching. In particular, we are going to make use of an experimental method developed by Dr. Ródenas et al.

As it was said before, this technique takes advantage of the chemical properties of the material and proposes to combine the role of a laser and the performance of a chemical etching.

A very basic sketch of the steps is represented in Figure (3.6).

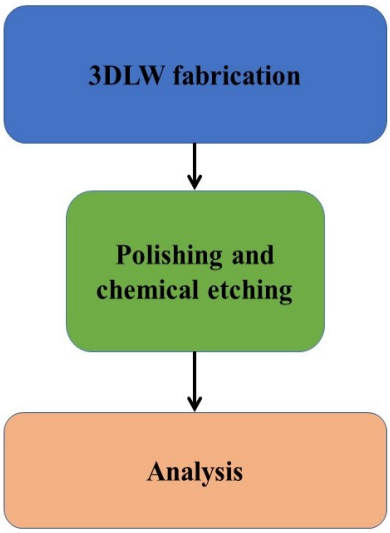

Figure 3.6: Summary of the experimental procedure.

The experimental setup required for this technique is fundamentally composed by four elements. See Figure (3.7).

1. **Femtosecond laser system (Fs-laser system)**.

   It is composed by a continuous wave laser (Millenia eV, Spectra-Physics) that pumps a fs-pulse laser (Ti:Sa Tsunami, Spectra-Physics). The latter works at a wavelength of $\lambda \approx 800\ nm$. It is very important to remain at this wavelength range because it is easier to focalise energy at the region of interest. If we did it at the UV range, photons would be too energetic and other areas could be accidentally modified.

2. **Selecting light components and pulse-picker system.**

   The first part of this system is composed by a device that separates vertical and horizontal components of light and allows us to remain with the vertical component.

   The pulse-picker device allows to select from the original fs-pulses, which are provided by the Ti:Sa Tsunami laser, a number of pulses or define a new pulse by using a "window system". So, at the output of the pulse-picker we can obtain pulses that are characterized by their pulse duration or width (number of pulses from the fs-laser that are in a window, given by time units) and the pulse repetition frequency (frequency units).

3. **Laser writing, nanopositioning and imaging system.**

   This part of the setup refers to the nearest zone to the sample. The first section is composed by a beam expander that, as its name indicates, increases the pulse width. Then, the beam passes through a microscope objective with a 1.42 numerical aperture (NA) oil-immersion into the sample.

   The sample is placed on a mobile platform that can be controlled via a com-

puter code program running in the Aerotech software (CODE.pgm). This allows the user to control certain parameters such as laser writing speeds or movements of the sample.

In some cases, it is necessary to have a quarter waveplate that provides circular polarization before the objective. This can be convenient because the orientation of the polarization is very important when a linear polarized beam impacts in something that moves. However, if light is circular polarized this fact is irrelevant because dependence the between platform movement (sample movement) and orientation of the polarization is eliminated.

4. **Polishing and study of the sample.**

Once laser writing has done, the sample has to be polished. To obtain this, a polisher machine is used. In order to avoid unpleasant movements of the sample while the laser writing is being done and for observing at the optical microscope, the crystal is stuck to a microscope slide using nail polish. So, before polishing, the sample has to be removed from the microscope slide by placing it in a ultrasound machine. When this task is done, the sample is dried using optical paper and put in the polisher machine. See Figure (3.8).

Then, a chemical composition made of H_3PO_4 and H_2O is prepared and poured in a beaker with the sample. Also, a magnetic stirrer is used with the objective of helping the acid to penetrate in the tracks. The idea is that the acid interacts with the modified parts of the material due to the laser and creates a hollow way giving rise to air pores.

Now the sample is ready to be analyzed.

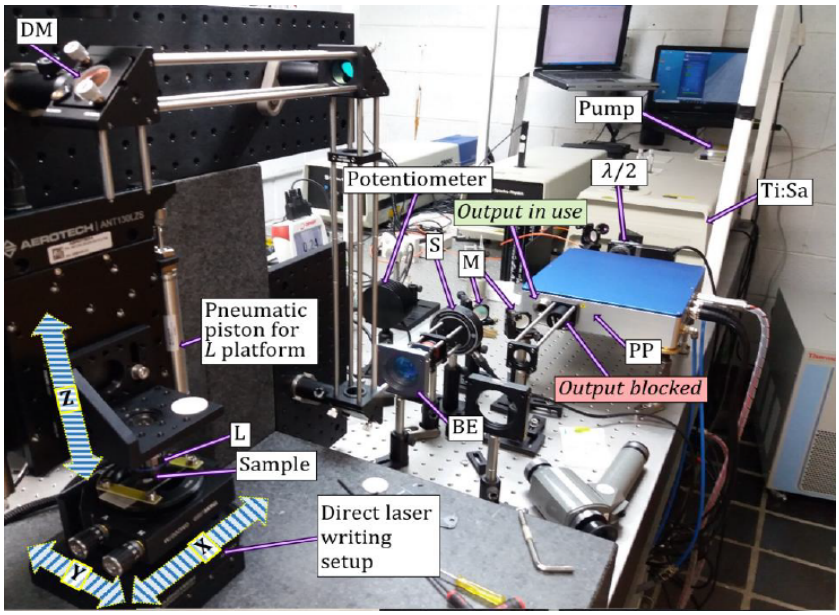

Figure 3.7: Experimental setup.

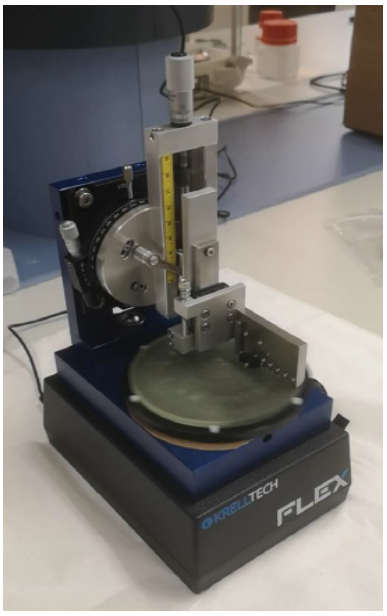

Figure 3.8: Polisher instrument.

3.3 SEM analysis.

Another task that we did was performed at the SEGAI facilities because the use of the scanning electron microscope was needed. This microscope is shown in Figure (3.11.)

The day before the observation, the sample was sent to the SEGAI with the purpose of adding a metal covering. This process is called “metal coating” and it is necessary for using this type of microscope. In our case, we covered the crystal in gold by a “sputtering” process with argon in gold and a Quorum Q150RS sputter coater was used. This instrumentation can be seen in Figure (3.9) and the user can configure some parameters such as time of the process or electrical current.

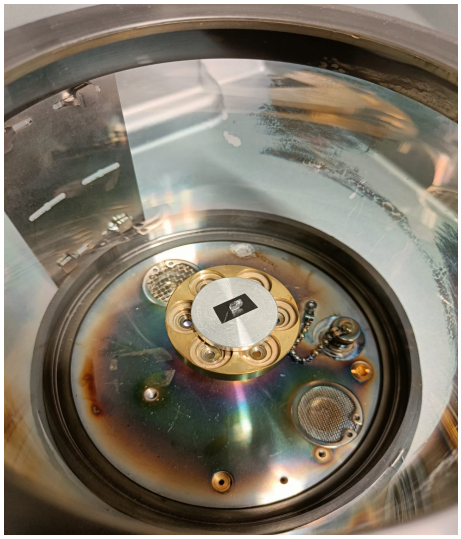

Figure 3.9: Sputter coater.

In a first attempt, a problem occurred. During the metal covering, the sample was

placed in a higher position than the expected one and also an elevated value of the current was applied. Due to this, the crystal was a bit burnt. To fix this, it was necessary to clean the sample by using an acid composition and acetone until the pores were perfectly visible and no metal covering remained. Figure (3.10) shows the behavior of the sputtering process by expressing a linear dependence between the deposition (process in which the metal coating adheres at the sample) and the deposition current as time passes.

After that, it was possible to make measurements with the scanning electron microscope. The sample was placed in a vacuum chamber and a computer was used to move around and observe the regions of interest. The image that the microscope provides is based in the scattering principle. The microscope itself sends energetic electrons to those which are present in the metal coating, making an energy transfer. So, the electrons of the coating are detached and detected by the microscope.

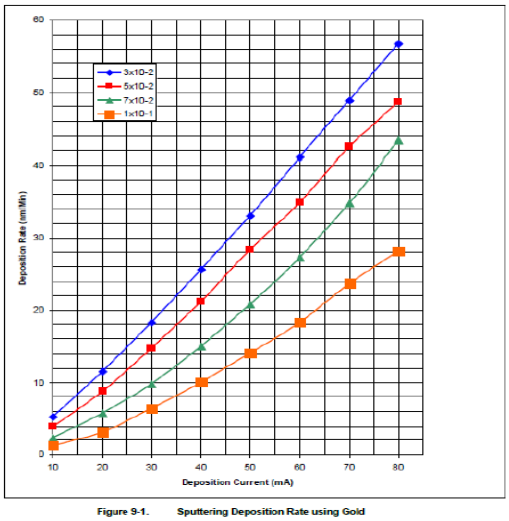

Figure 3.10: Plot sent from the SEGAI that shows the development of the metal coating. x-axis shows the deposition current and y-axis shows the deposition rate.

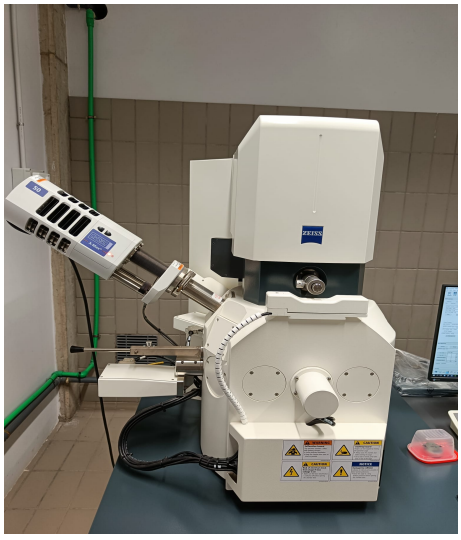

Figure 3.11: Scanning electron microscope.

Chapter 4

Analysis and results.

En esta sección se presentan de manera breve los procedimientos utilizados para obtener los resultados. Se comienza analizando algunas de las características obtenidas en los experimentos de laboratorio y se continúa discutiendo los resultados obtenidos en la simulación hasta llegar al diseño de la guía de ondas. Todos ellos se muestran de la manera más ilustrativa posible recurriendo a gráficas y tablas.

4.1 Pore length study.

4.1.1 Preparing the sample to be observed.

Once the sample was ready to be analyzed, a use of the Raman microscope was needed to determine some of the parameters of interest.

The first value to be obtained was the length of the pores that were etched after the chemical attack. In order to achieve that objective, it was necessary to observe the sample in transmission, not in reflection. The key point was to use an external light that fell on the sample from behind.

As the whole sample did not fit in all the microscope's field of view, it was necessary to examine it part by part. The first idea that came up to us was to use a function of the computer program which generated a montage. However, after some failed attempts in which the image did not focalize, we decided to build it manually. So, we took pictures of different parts of the sample and labeled them to make easier the process of locating them in the complete rebuilt-in picture.

After that, knowing the exact order of the pictures that were taken, we used the ImageJ [8] program to measure directly the length of the pores. First of all, an equivalence between pixels and real distances was set and, after that, measuring the length was as simple as drawing a straight line over the pores.

Also, as the CODE.pgm program was run in the Aerotech software, knowing the laser writing speeds was possible by just reviewing the configuration that was set by the moment when pores were written.

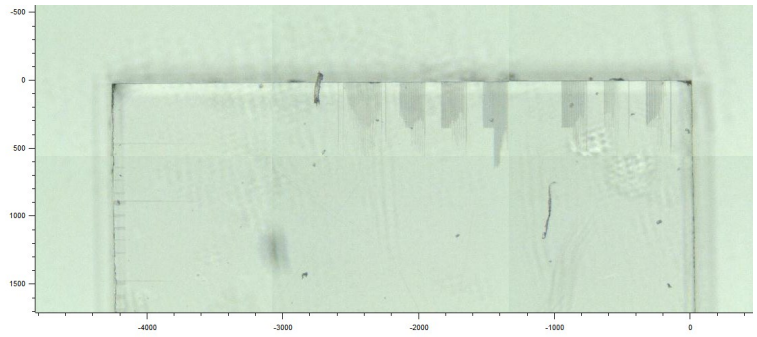

(a) Montage of the whole sample. This picture is shown just to get a visual idea of the pores distribution and no measurements were made in it.

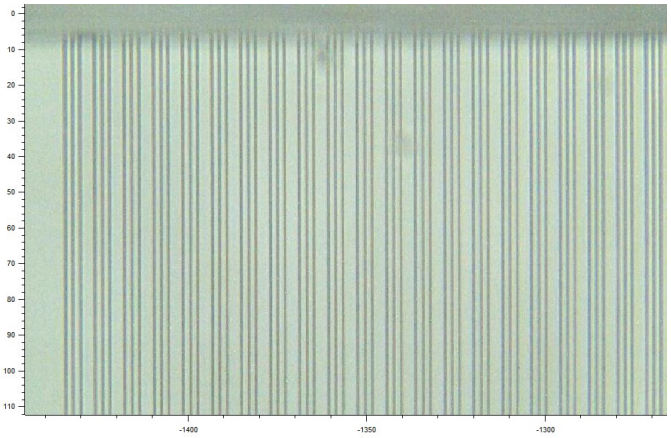

(b) Example of one of the pictures used for measuring pore lengths. It can be seen that there are three tracks together, they correspond to going, return and going and return tracks.

Figure 4.1: Pictures of the sample.

4.1.2 Repetition frequencies of the order of kHz.

Keeping in mind that there were different laser repetition frequencies and pulse energies, Figure (4.2) and Figure (4.3) were obtained. These are representations that contain the laser writing speeds in the x-axis and the length of the pores after the chemical etching in the y-axis for different repetition frequencies and energies. Also, the laser writing length is represent by the grey line.

As it can be seen, there is a dependence between the repetition frequency, laser writing speeds and the pore length. First of all, it is noticeable that the higher writing speed, the shorter the pore length. A possible explanation would be in terms of pulse densities. If the writing speed is low, the energy received by the laser is well concentrated in a region. So, a considerable modification in the material is done. Consequently, it is easier for the acid to lead the way. However, if writing speeds are too high, the amount of energy per region is lower and the modification in the crystal is not that noticeable. Therefore, the acid can not cover long distances. Also, the "overlapping" between laser marks (which constitute a track) is important for chemical etching and consequently, the pore length. If writing speeds are very

high, it is possible for low repetition frequencies that marks do not touch each other and acid can not pass through, creating a hollow path. Also, this could be the reason of the decreasing behavior at fast speeds. A remarkable example would be the $f = 1kHz$ and $E = 20\ nJ$ case. Having the lowest repetition frequency, at fastest speeds the accumulation of energy pulses is not enough to make a considerable modification in the material. This could be the reason of the absence of measurements at higher speeds than 0.5 mm/s. But, as it was said before, also the non-overlapping event can affect.

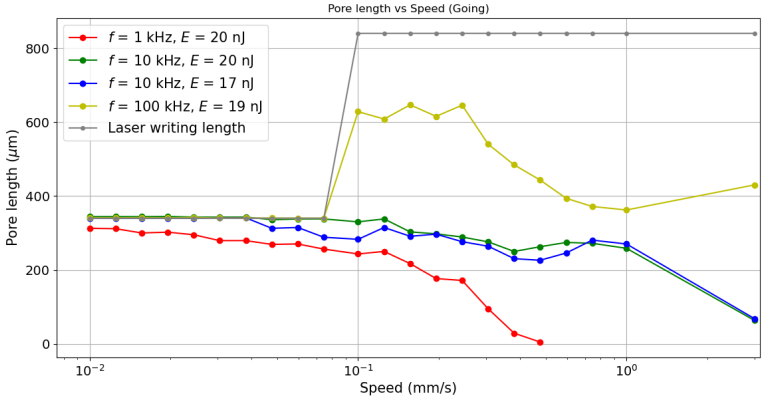

(a) Pore length for each laser writing speed I.

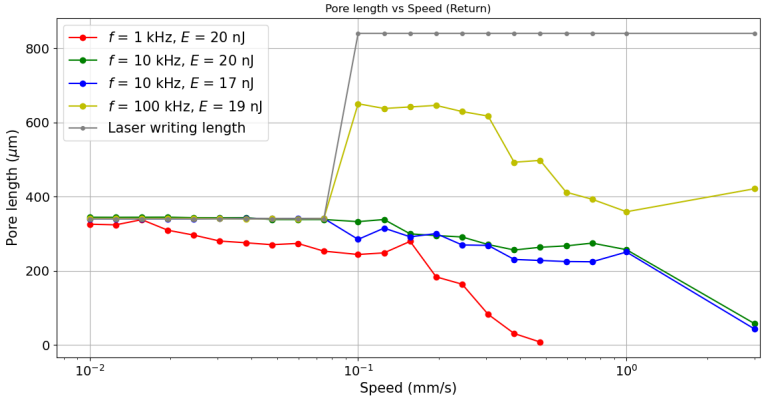

(b) Pore length for each laser writing speed II.

Figure 4.2: Plot of the pore length and laser writing speed using a frequency of the order of kHz.

Another fact that can be observed is the dependence with the repetition frequency. The higher the frequency, the larger pore length. This can be explained because for a fixed laser writing speed, if the frequency is higher, the number of pulses that reach the sample is greater. This involves a bigger amount of energy per region and better marks of the laser which leads to a better chemical etching.

An interesting result can be obtained from these cases: (1) $f = 10\ kHz$, $E = 20\ nJ$; (2) $f = 10\ kHz$, $E = 17\ nJ$ (Blue and green line in Figure (4.2)). As it can be seen, both have the same frequency but different energies. However, the behavior is mostly the same. This seems to indicate that the dependence between pore length and repetition frequency is stronger than between pore length and energy.

It is important to mention that, apparently, there is a saturation region at $\approx 340\ nm$ where the pores are not longer. This can be explained because tracks made by the laser were 340 nm long, so when the acid reached that point, it was the end of its path and could not continue creating a hollow way.

4.1.3 Repetition frequencies of the order of MHz.

Also, we can get similar results for frequencies of the order of MHz. See Figure (4.3). These pores were written using different laser writing speeds. As it can be seen, the maximum writing speed is higher than for the other measurements. This is because, in this case, the frequency is larger enough, so the accumulation of energy is still being the same, despite faster speeds. Also, from these plots we conclude that the $f = 1\ MHz, E = 17nJ$ case was the best to determine the 3 different regimes or regions that can exist in this procedure. Zone 1 shows from right to left an increasing nanocrack density. This means that the stress produced in the material is low and modifications are not noticeable. Zone 2 represents a maximum region which gives us the optimal writing speed that provides the longest pore lengths. Finally, studying Zone 3 it is possible to see that, the higher the writing speeds, the lower the energy accumulation, so the shorter the pore length.

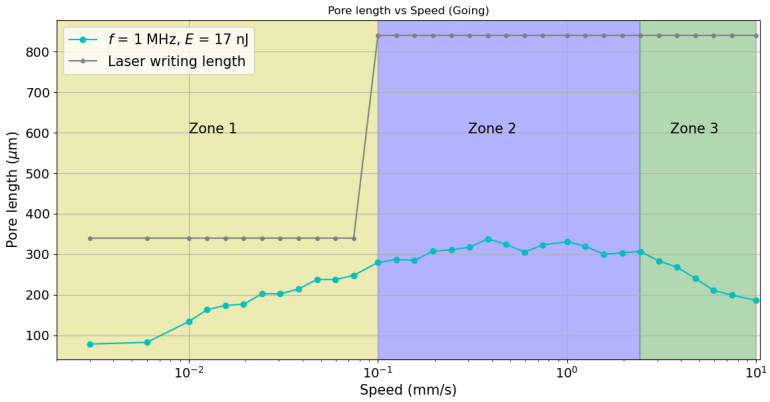

(a) Pore length for each laser writing speed I.

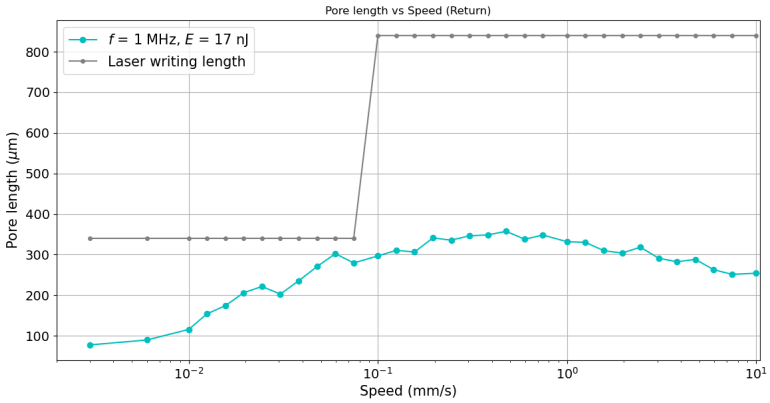

(b) Pore length for each laser writing speed II.

Figure 4.3: Plot of the pore length and laser writing speed using a frequency of the order of MHz.

4.2 Analyzing SEM images.

After the study of the length of the pores, it was necessary to analyze the cross-sectional plane. To achieve this goal, SEM pictures were analyzed. It is important to mention that, in this project, we were not able to measure in the sample mentioned in Section (4.1) because of some technical problems that occurred at SEM facilities and caused delays. So, for the purpose of learning the measuring method, we used some images provided by Dr. Ródenas and taken by himself last year. The characteristics of these images are the following.

a) Repetition frequency: $1MHz$.

b) Writing speed: $1\ mm/s$.

c) Laser power: decreasing 4 by 4 from left to right.

By using the ImageJ program and following some formally established steps by Dr. Ródenas, we were able to measure the widths and the heights of the pores. To do this, we approximated the cross-sectional shape of the pores as ellipses.

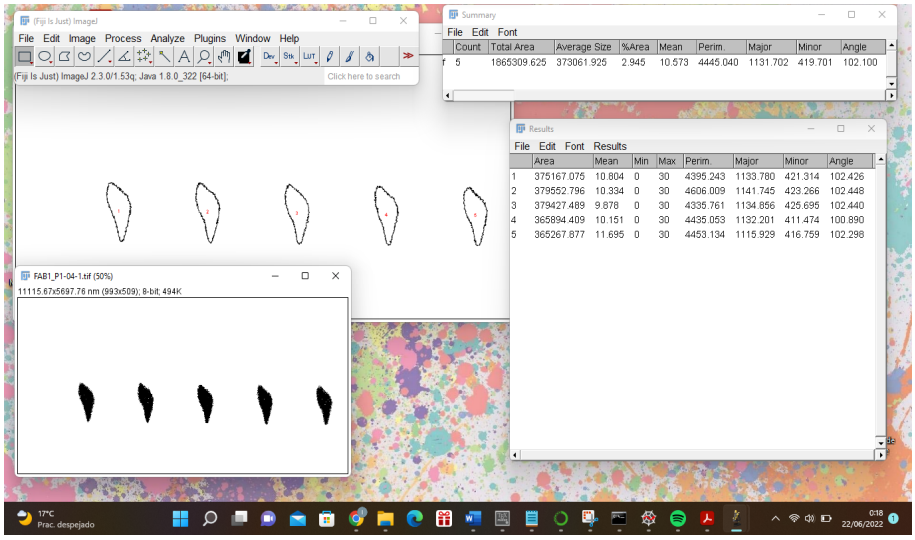

Figure 4.4: Screenshot of an image analysis by using ImageJ.

So, the following results were obtained.

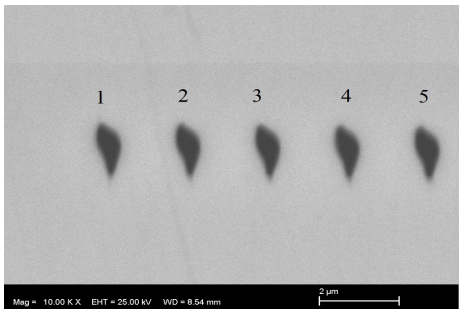

Figure 4.5: SEM image obtained using the scanning electron microscope.

Table 4.1: Results of Figure (4.5)

Pore	**Major axis** (μm)	**Minor axis** (μm)
1	1137.71	422.87
2	1145.91	424.61
3	1138.82	427.26
4	1135.86	413.09
5	1119.21	414.21

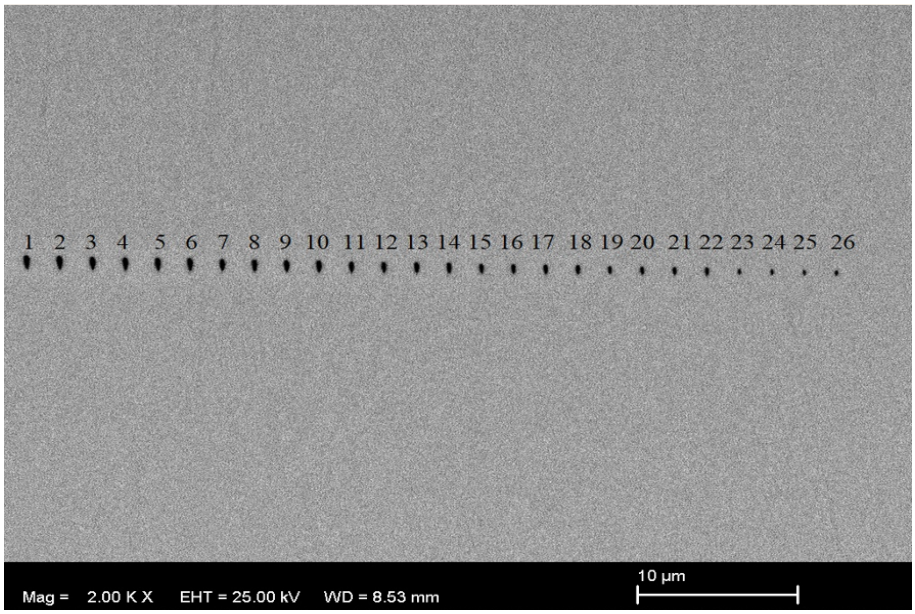

Figure 4.6: SEM image of a nanopores array.

Table 4.2: Results of Figure (4.6).

Pore	**Major axis** (μm)	**Minor axis** (μm)	**Pore**	**Major axis** (μm)	**Minor axis** (μm)
1	898.96	318.27	**14**	642.12	247.54
2	840.27	335.77	**15**	566.47	224.48
3	844.08	296.60	**16**	605.48	223.14
4	803.61	306.59	**17**	605.33	229.77
5	810.71	294.10	**18**	560.73	233.80
6	811.00	289.09	**19**	458.77	181.90
7	741.83	273.19	**20**	483.01	181.00
8	750.94	280.46	**21**	493.33	217.49
9	732.97	292.76	**22**	476.99	216.60
10	788.10	282.37	**23**	292.12	122.43
11	714.26	250.36	**24**	327.09	133.64
12	670.92	260.61	**25**	321.60	185.34
13	689.41	259.38	**26**	362.91	208.04

Attending to these results, it can be confirmed that, the lower the laser power, the smaller the pores. This is noticeable in Table (4.2).

4.3 2D Photonic Hexagonal Lattice.

Another task which was successfully completed was the optimization of a 2D hexagonal lattice. The structure was a periodic array of air holes with lattice constant $a = 1\ \mu m$ within a material with different refractive indexes whose values will be shown later. The main objective was to find the best configuration of the lattice (find the appropriate pore width or diameter) in order to get the widest bandgaps for TM and TE polarization. To achieve this, a use of the simulation program BandSOLVE was needed.

Note: BandSOLVE software convention indicates that TE polarization corresponds to the electric field pointing out of the 2D plane and magnetic field within the plane. However, TM is the opposite and the one of interest for Photonic Crystal Waveguides (PCWs) fabrication [9].

4.3.1 Setting up the structure to be analyzed.

The first step of the procedure was to find the value of the refractive index for different ranges in the electromagnetic spectrum. As we wanted to carry out our analysis in the UV (Ultraviolet), VIS (Visible), NIR (Near-infrared), MIR (Mid-wavelength infrared), the following refractive indexes were found. See Table (4.3).

Table 4.3: Refractive index for different ranges in the EM spectrum [10].

EM spectrum	Wavelength (nm)	Refractive index
UV	250	1.9618
VIS	530	1.8383
NIR	1500	1.8077
MIR	5000	1.7720

Also, the most common configuration of YAG crystals was studied.

$$\boxed{\lambda = 1000\ nm\ ;\ n = 1.8}$$

Given these values, it is clear the dependence of the refractive index as a function of the wavelength $n = n(\lambda)$. The larger the wavelength, the smaller refractive index.

Once these values of the refractive index were stored, the following step was to implement the MOST function of the BandSOLVE software. This function performs a high number of calculations of bandgaps and their characteristics along the reciprocal lattice while varying one parameter that we choose. See Figure (4.8). In this case, the parameter to be changed was the pore width.

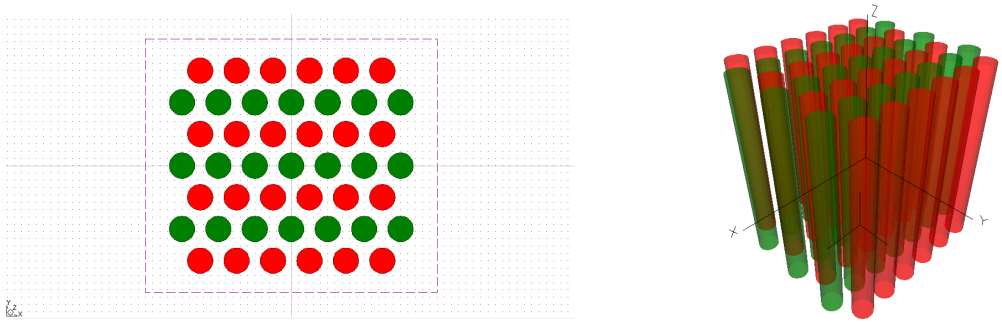

(a) Cross sectional XY plane of the structure.

(b) 3D diagram of the structure.

Figure 4.7: Hexagonal structure to be optimized. Despite it is shown a 3D model, the study will be performed along the 2D cross-sectional plane. The refractive index and the index contrast were settled down in the software in order that red and green rods represent the air holes and the rest of the set up is the material.

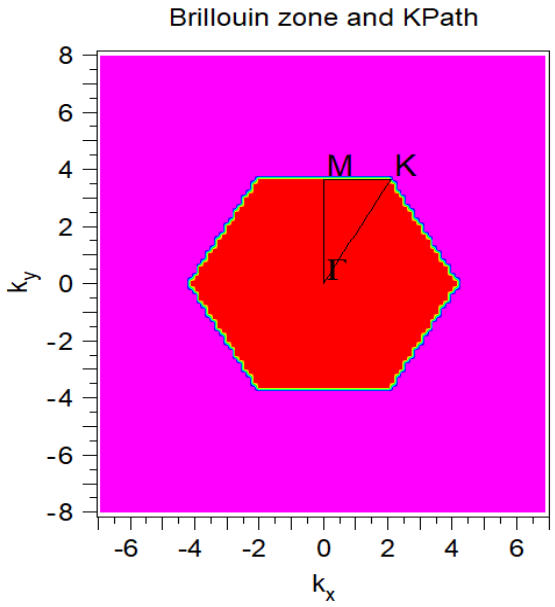

Figure 4.8: Reciprocal lattice of the 2D hexagonal lattice. Also the symmetry points where the eingenvalues were calculated are shown (Γ, M, K).

Figure (4.9) shows an example of a band diagram of this structure. The periodic pattern is a hexagonal array of air pores studied in the UV region, so the wavelength is $\lambda = 250\ nm$ and the refractive index corresponds to $n = 1.9618$. As it can be seen in this band diagram, there is a fundamental bandgap[1] of TM polarization at a normalized frequency of $f \approx 0.47$ and a higher order bandgap for TE polarization at a normalized frequency of $f \approx 1.07$.

We wanted to emphasize again that the polarization of interest for fabricating PCWs is TM because it is the one where the field is polarized transverse to the waveguide, i.e. polarization direction contained in the plane of the periodic hexagonal structure.

[1]Fundamental bandgap: as its name indicates, it is a bandgap that appears between the 0^{th} order and the 1^{st} order band

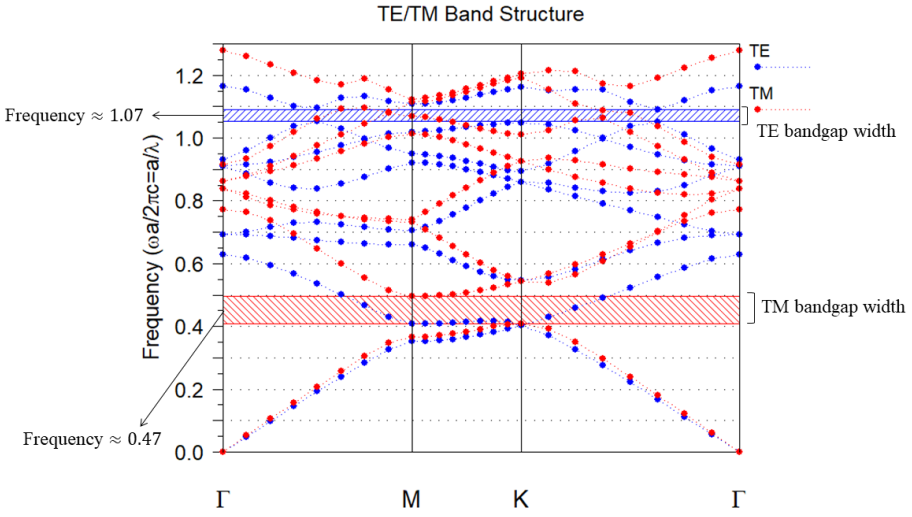

Figure 4.9: Band diagram example of a hexagonal lattice with $a = 1\ \mu m$ and a 0.8 μm pore diameter. It is studied at the UV region with a wavelength of $\lambda = 250\ nm$ and a refractive index $n = 1.9618$.

4.3.2 Optimization process results.

After implementing the MOST function, the results obtained are shown in Figure (4.10). Also, both gap width (TM and TE) were plotted. See Figure (4.11) and Figure (4.12).

All these graphics correspond to a file which contains the exact coordinates of the data in the plot. Studying those files, we concluded the following results. See Table (4.4) where the ideal pore diameter for each refractive index is shown. Also the band diagrams of the optimal configurations are shown in Figure (4.13).

Table 4.4: Results of the optimization process for different wavelengths and a lattice constant of $a = 1\ \mu m$.

Wavelength and refractive index	Pore diameter (μm)
$\lambda = 250\ nm$ n = 1.9618	0.81
$\lambda = 530\ nm$ n = 1.8383	0.79
$\lambda = 1500\ nm$ n = 1.8077	0.78
$\lambda = 5000\ nm$ n = 1.7220	0.78

By looking Table (4.4), it can be seen that the optimal diameter is longer for bigger refractive index.

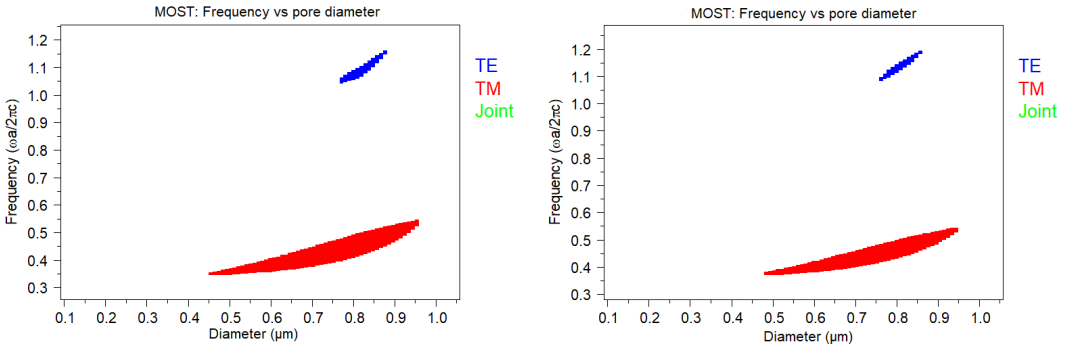

(a) $\lambda = 250\ nm$ and $n = 1.9618$.

(b) $\lambda = 530\ nm$ and $n = 1.8383$.

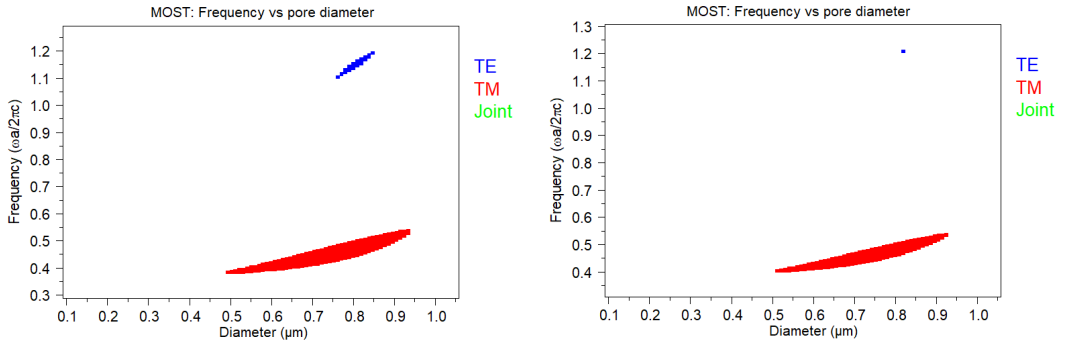

(c) $\lambda = 1500\ nm$ and $n = 1.8077$.

(d) $\lambda = 5000\ nm$ and $n = 1.7220$.

Figure 4.10: Gap map for different EM spectrum ranges and their respective refractive index.

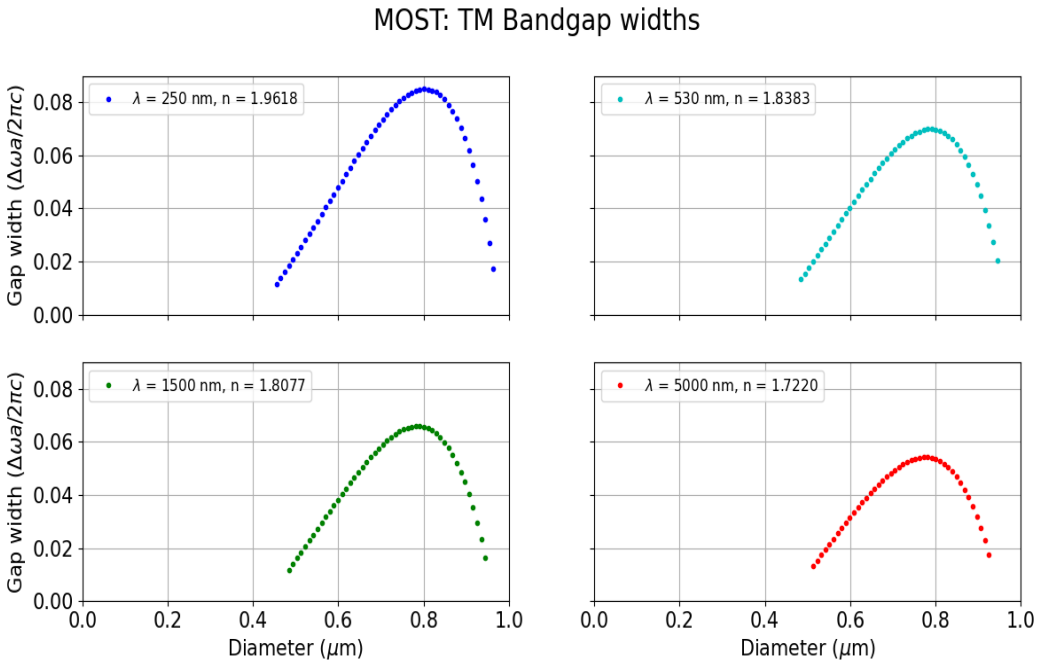

Figure 4.11: Optimization process results. Gap width as a function of the pore diameter for TM polarization.

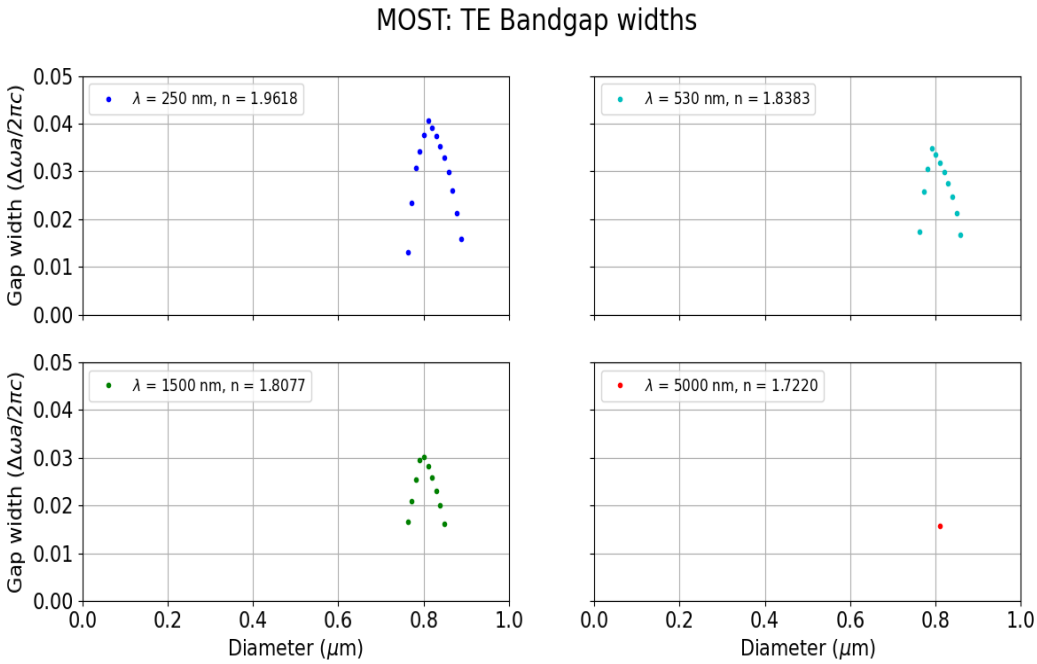

Figure 4.12: Optimization process results. Gap width as a function of the pore diameter for TE polarization.

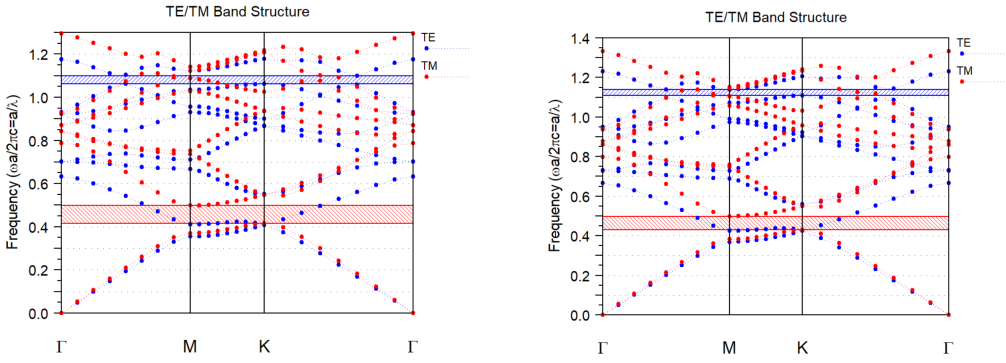

(a) $\lambda = 250\ nm$ and $n = 1.9618$.

(b) $\lambda = 530\ nm$ and $n = 1.8383$.

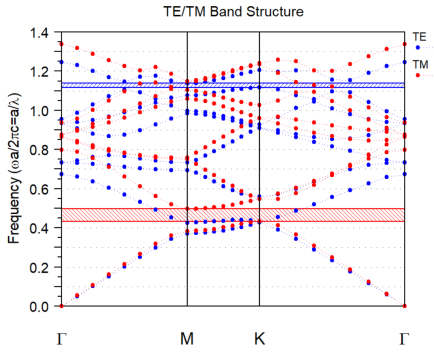

(c) $\lambda = 1500\ nm$ and $n = 1.8077$.

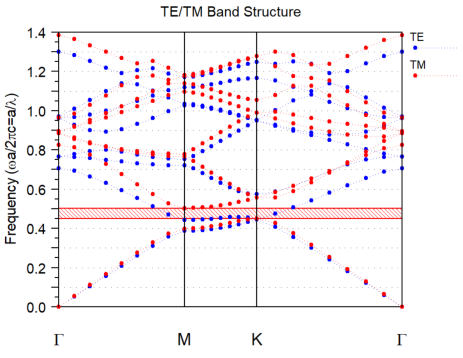

(d) $\lambda = 5000\ nm$ and $n = 1.7220$.

Figure 4.13: Optimal band diagrams for different EM spectrum ranges and their respective refractive index.

These results will be very important, not only for the following Section (4.4), but also they can be applied in experimental structures which can be obtained in the laboratory. An example of an experimental structure can be seen in Figure (4.14).

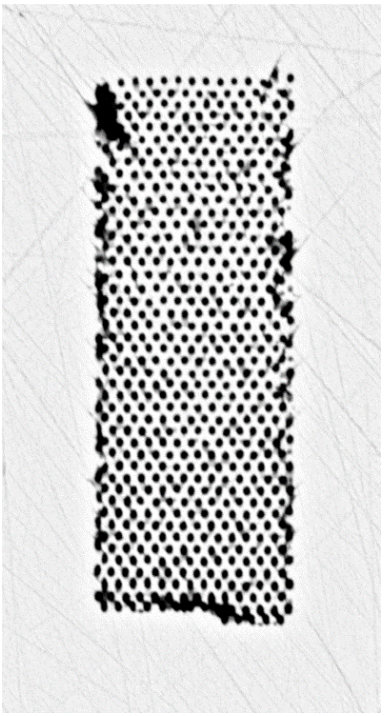

(a) Array of nanopores.

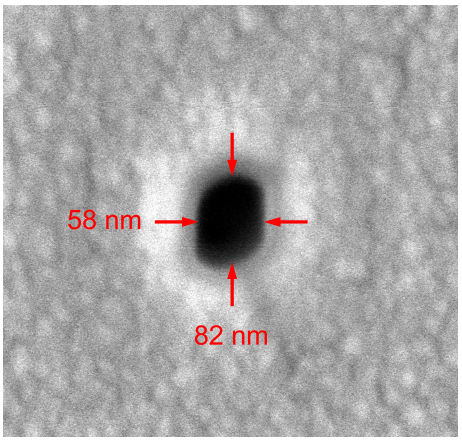

(b) Transversal plane of one pore.

Figure 4.14: Hexagonal lattice fabricated by Dr. Ródenas. Spacing of 250 nm.

4.4 Microstructured Optical Waveguide (MOW).

As a technological application of this technique, it is remarkable the fabrication of a microstructured optical waveguide. So, in this section, the study of one of them will be carried out.

There are different types of waveguide designs. In this case, we will study an array of microscopic air holes that guides light in a defect within the periodic pattern with a lattice constant of $a = 1\ \mu m$. The light propagates in the form of modes. These are the different ways in which light passes through a waveguide in general and there is a finite number of them. Each mode is associated to one normalized frequency. If the waveguide supports only one mode it is known as "single-moded".

To do this task, it was necessary the use of the BandSOLVE software one more time. The structure which was used during the whole analysis is shown in Figure (4.15) and its physical parameters are displayed in Table (4.5).

Table 4.5: Microstructured optical waveguide parameters.

Parameter	Value
Wavelength (λ)	1000 nm
Refractive index	1.816
Period (a)	1 μm

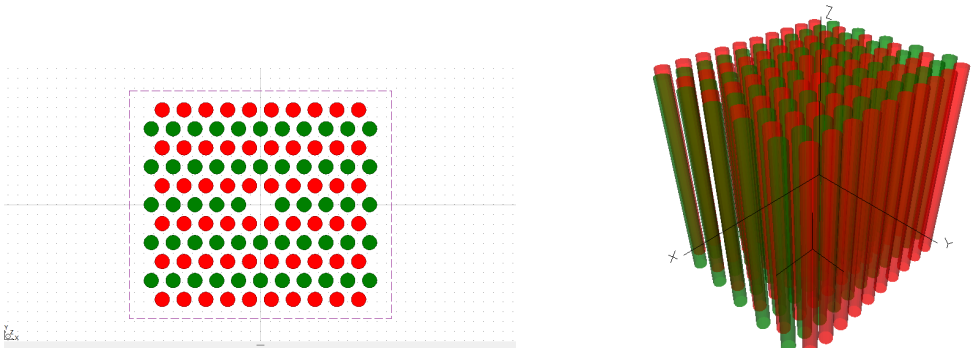

(a) 2D (XY) plane of the MOW. The perpendicular direction is defined along the z-axis.

(b) 3D model of the MOW.

Figure 4.15: Hexagonal structure which represents a MOW. There is a defect core in the middle.

4.4.1 Mode profiles analysis.

First of all, intensity mode profiles were observed. To achieve this, a hexagonal cell was used at first but then, it was changed to a square cell in order to separate the defects a reasonable distance when the whole periodicity of the lattice is considered. During this process, we learnt that defect modes have flat bands and due to this, it is sufficient to resolve Equation (3.3) only in one symmetry point. As it is known, light propagation in a waveguide is carried out along the longitudinal axis of it. So, the point of symmetry chosen for the study was the one with $(x, y, z) = (0, 0, 10)$ coordinates.

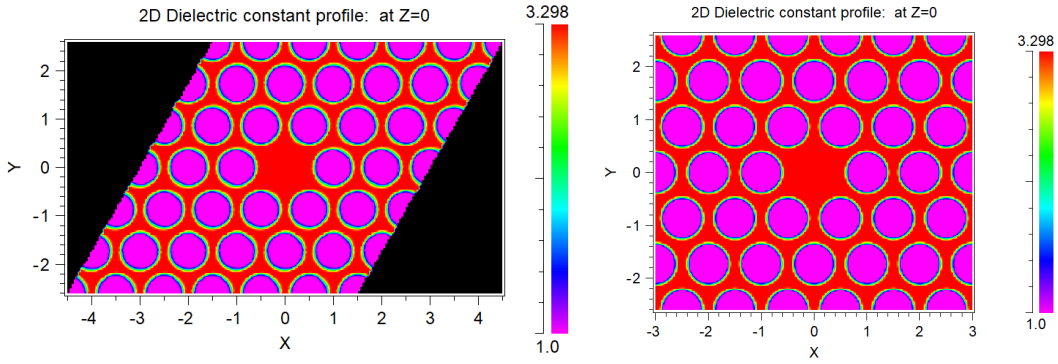

(a) Hexagonal cell domain.

(b) Square cell domain.

Figure 4.16: Unit cell domains.

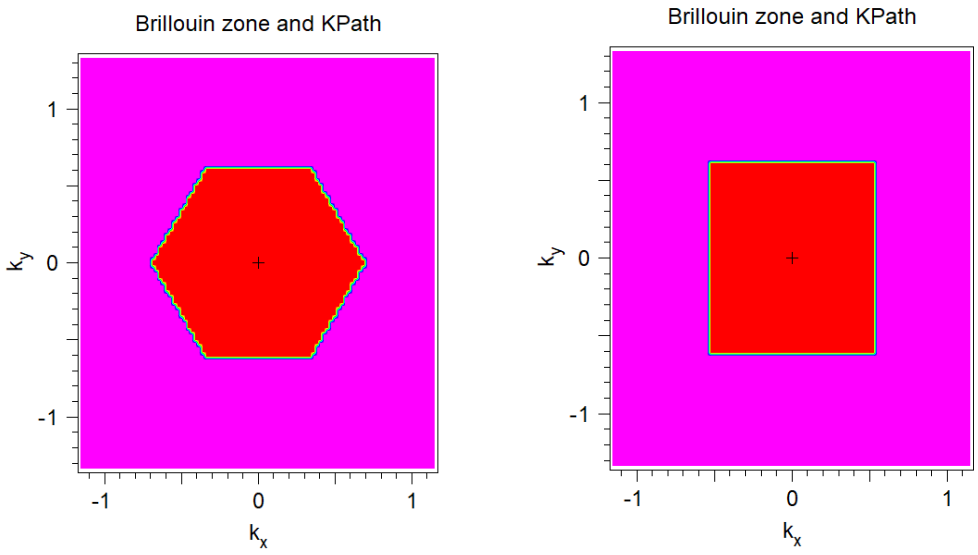

(a) Brillouin Zone for a hexagonal cell. (b) Brillouin Zone for a square cell.

Figure 4.17: Brillouin Zone for each cell domain. The point where eigenvalues and eigenvectors were calculated is also represented.

Also, we found out the relation between the refractive index of the modes (n_{eff}) or "effective index" and their frequency (f_{mode}) [9].

$$n_{eff} = \frac{|k|}{\omega} \tag{4.1}$$

Where:

- $|k|$: modulus of the wave vector (μm^{-1})
- ω: frequency of the mode $\omega = \frac{2\pi c}{\lambda} = 2\pi f_{mode}$ (rad/s)

Following the definition of a MOW, we are interested in light which propagates within the defect. The defect core is a high index region. So, those modes confined in the core will have a high refractive index. Looking at Equation (4.1), it is reasonable that confined modes have lower frequencies, in other words, they are the lowest order modes. BandSOLVE software solves Equation (3.3) obtaining the eigenvectors and eigenfrequencies from the lowest to the highest. Taking advantage of this, for our purpose, we asked him to resolve only a small number of them. So, four eigenvalues were obtained.

Modes that have a lower refractive index are those which extend into the cladding. As this cladding is filled with air holes, in average, its refractive index is decreased. This modes are known as "cladding modes" or radiation modes. So that, they will have a lower refractive index and, consequently, a higher frequency.

Keeping all this concepts in mind, Figure (4.18) shows the obtained results at a wavelength $\lambda \approx 1\ \mu m$.

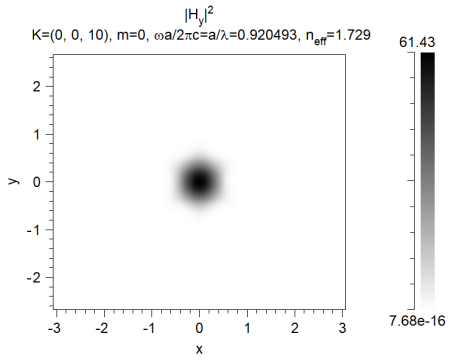

(a) Fundamental mode (I) $\lambda = 1086\ nm$.

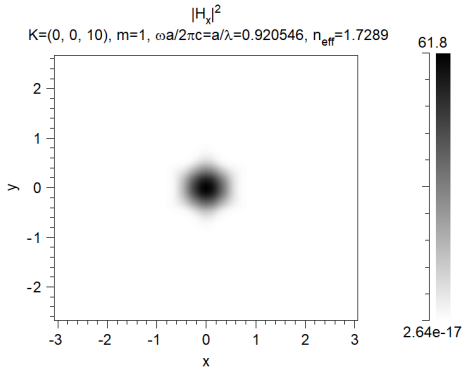

(b) First order mode (II) $\lambda = 1086\ nm$.

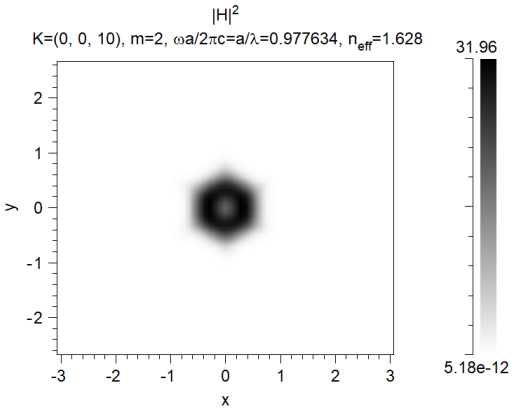

(c) First higher order mode $\lambda = 1023\ nm$.

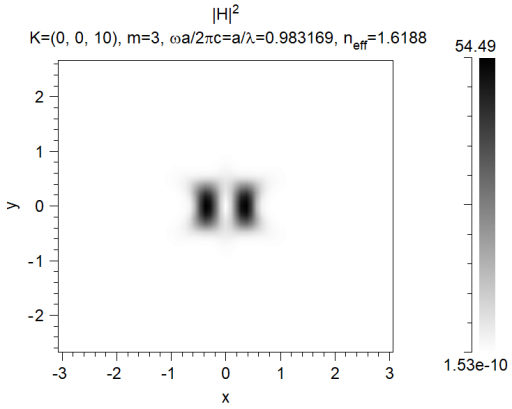

(d) Second higher order mode $\lambda = 1017\ nm$.

Figure 4.18: Intensity mode profiles.

From these results it is confirmed the existence of several confined modes of different orders. This can be seen because of the absence of light outside the core. Also, it is remarkable that the fundamental mode is a degenerate polarization state. In other words, both modes are the same but one of them is polarized along the x-axis and the other one is polarized on the y-axis. For this reason, the square modulus of only one component of the magnetic field ($\vec{H}$) was plotted. The other component in each mode would be almost non-existent. The higher order modes are polarized along both axes, so it is better to show the total intensity, which is a contribution of both components.

Note: during the study of the mode profiles, we realized that we did not observe mode profiles at the frequency where the maximum TM bandgap was located, i.e., a normalized frequency of ≈ 0.47. To do this, the study of the mode profiles should have been done at a wavelength of $\lambda \approx 2\mu m$.

Also, from these calculations it was possible to obtain the effective index of the modes and their spatial width. See Figure (4.19). As it can be seen using Figure (4.18), those modes with a higher effective index are confined the most within the defect. For this reason, the refractive index observed by these modes is closer to the material refractive index than the others. Modes that are not that confined see its refractive index decreased because of the presence of air holes. Also, it is logical

that more confined modes have a smaller spatial width than those which not.

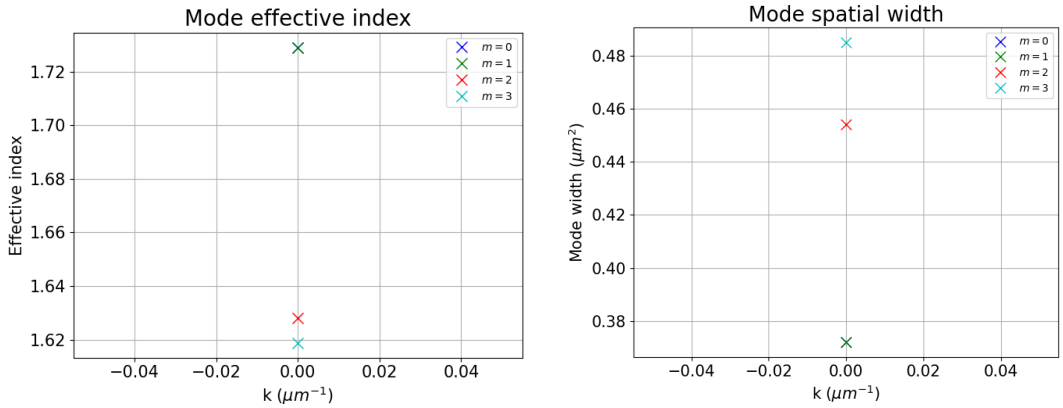

(a) Mode effective index. (b) Mode spatial width.

Figure 4.19: Results obtained from BandSOLVE simulator.

4.4.2 Study of dispersion relations.

After that, we tried to obtain some dispersion relations. To achieve this, it was necessary to calculate the normalized frequency for different wavelengths. So, an optimization process was developed using MOST function. As result, we obtained Figure (4.20).

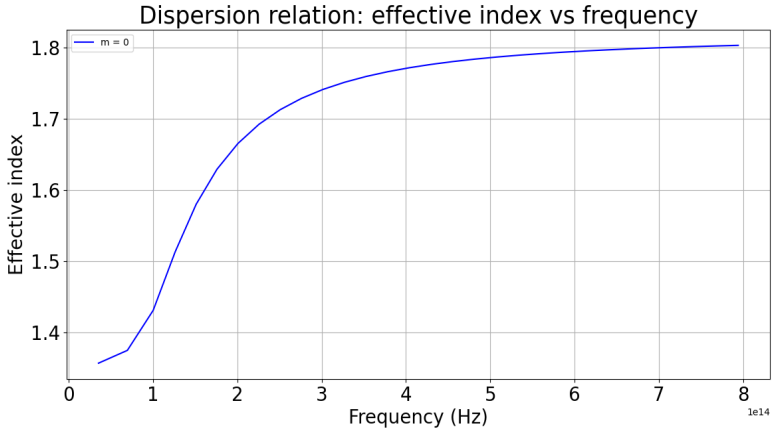

Figure 4.20: Dispersion relation of the effective index and frequency.

From this part of the study, the most important fact was that we were able to obtain a plot of the effective refractive index as a function of wavelength. The main advantage of doing this is that we can see the effective index of the modes in a wide range of the EM spectrum, from UV to IR. See Figure (4.21). We decided to go further and compare the effective index function to YAG refractive index [10], obtaining an interesting result. This plot represents the behavior discrepancy between both indexes. Modes effective index decreases while wavelength increases. This tendency seems to be logical because, as the wavelength of light increases, it is more difficult for modes to be confined within the defect. In other words, for higher

wavelengths, light spreads out into the air hole array producing that pronounced decreasing behavior in the effective index. Despite the fact that YAG refractive index function also decreases with wavelength, the behavior is not the same. The reason is that this one follows the dispersion relation expressed in Equation (4.2) which is independent of whether the existence of a periodic array of air holes.

$$n^2 - 1 = \frac{2.28200\lambda^2}{\lambda^2 - 0.01185} + \frac{3.27644\lambda^2}{\lambda^2 - 282.734} \tag{4.2}$$

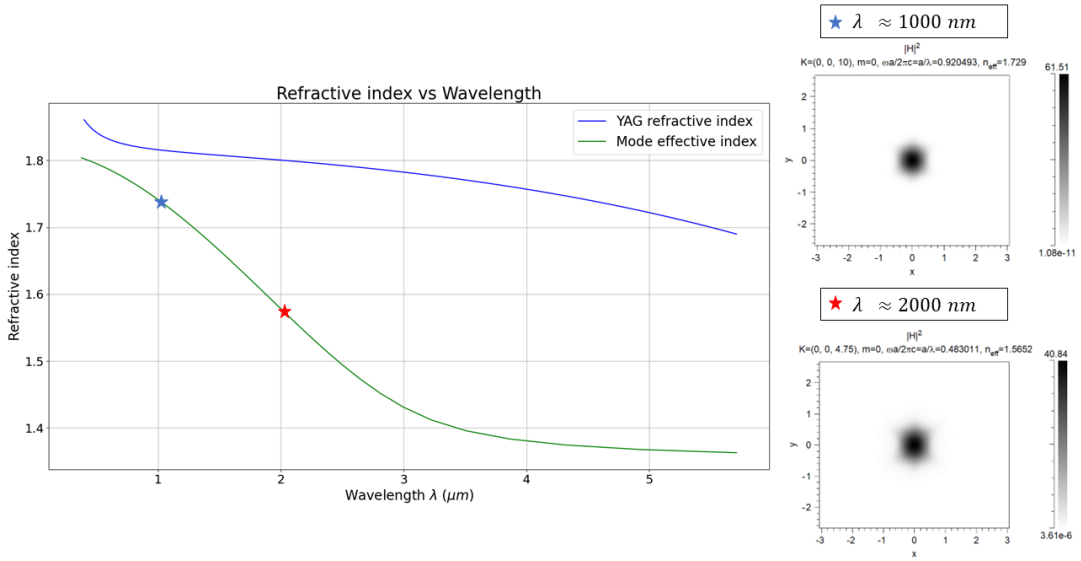

Figure 4.21: Comparison between modes effective index and YAG refractive index of the material. Also mode profiles for different wavelengths are shown at the right side of the plot.

We also see in this plot that at 2 μm, where the photonic bandgap lays, the dispersion of the modes is continuous. We expect that the presence of the PBG will impact losses of the modes which can be analyzed by looking a the imaginary part of the effective index. However, this is out of the scope of the present work and different type of numerical analysis is required.

4.4.3 Study of the number of confined modes.

As final task, a single-mode condition analysis was carried out. As it was said before, this implicates that the MOW supports only one mode of propagation. So, our goal was to look for the value of certain parameters of the MOW that led to that condition. The pore width was fixed at 300 nm, as it was considered a realistic value which can be obtained in a laboratory.

To begin with this last assignment, we used Equation (4.3). This expression is used for conventional MOWs with the purpose of determine the number of confined modes. For very small wavelengths, this number approaches infinity. However, in photonic crystal waveguides, V_{number} converges to a finite value when wavelength

decreases. If this value converges to a number less than 2.405 the PCW is single-moded. [9]

$$V_{number} = 2\pi \frac{\Lambda}{\lambda} \sqrt{n_0^2 - n_{eff}^2} \tag{4.3}$$

Where:

- V_{number}: number of confined modes.
- Λ: separation between pores.
- λ: wavelength of light.
- n_o: refractive index of the material.
- n_{neff}: "effective cladding index" (refractive index of the lowest mode in the band structure of the plain lattice)

Bearing in mind these concepts, we did an optimization process taking different values of wavelength and we looked at the smallest possible values of it in order to calculate the value that Equation (4.3) approached.

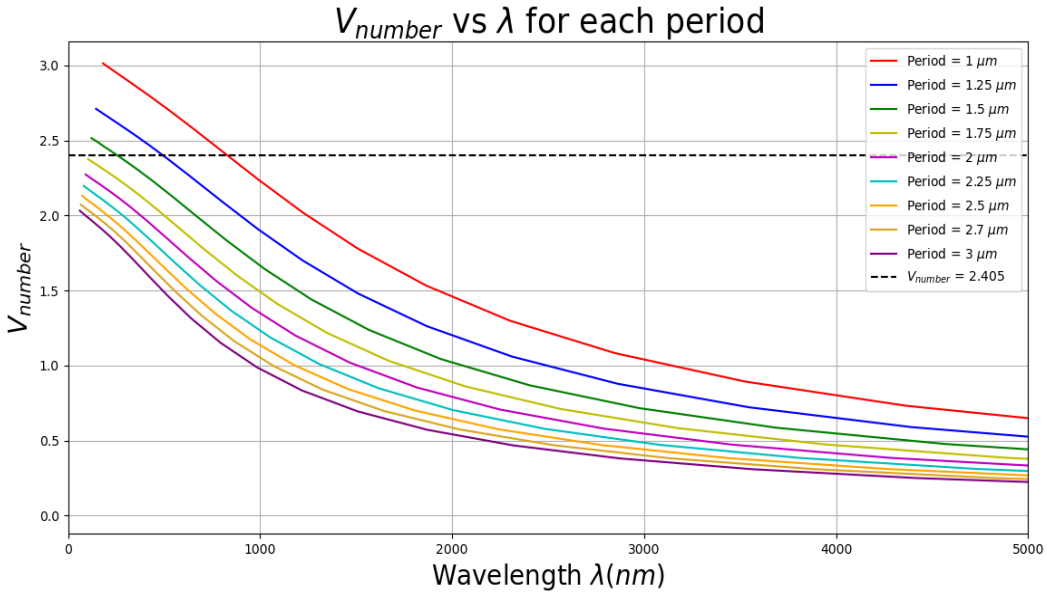

Figure 4.22: Values of V_{number} as function of the wavelength.

As it was expected, V_{number} decreases for increasing values of wavelength. This can be explained because the larger the wavelength, it is more difficult for light to be confined in the core. Consequently, the number of confined modes decreases. Attending to V_{number} rule, which was mentioned before, and looking at Figure (4.22), it seems that for a 1.75 μm period the waveguide is single-moded. So, we decided to compare the results of two simulations. In one of them, it was used a period which, apparently, the waveguide was single-moded. In the other one, we set up a period which, clearly, the waveguide was not single-moded. The stunning thing was that, despite the fact of the V_{number} criterion, the period that seemed to provide a non-single-moded waveguide, did it. We found this fact because, at some point, it

seemed that a "leaky mode" was found. This kind of modes look very similar to a confined mode but there is a maximum of intensity also outside the core. Figure (4.24a) illustrates this fact very well. We wanted to get more details about this special type of mode so, we increased the size of the study cell to see if this result was a confined mode or a numerical remainder of the software. The reason of doing this is that, sometimes, a small cell does not provide enough information of the whole lattice.

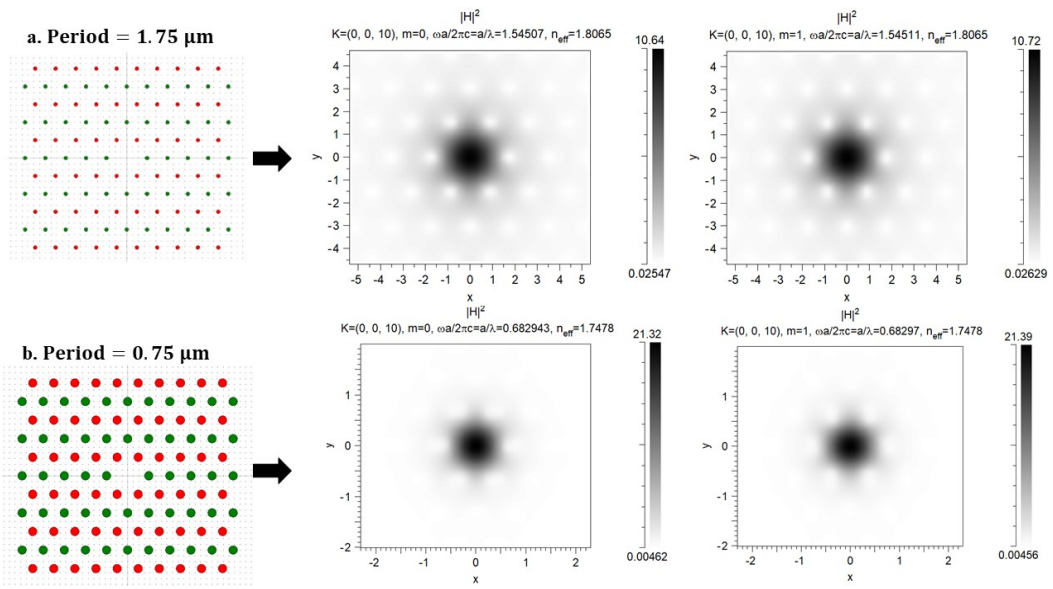

Figure 4.23: Fundamental modes for different lattice constants. **a,** Lattice period $a = 1.75\ \mu m$ and its fundamental modes at, from left to right $\lambda = 1133\ nm$ and $1133\ nm$. **b,** Lattice period $a = 0.75\ \mu m$ and its fundamental modes at, from left to right $\lambda = 1098\ nm$ and $1098\ nm$.

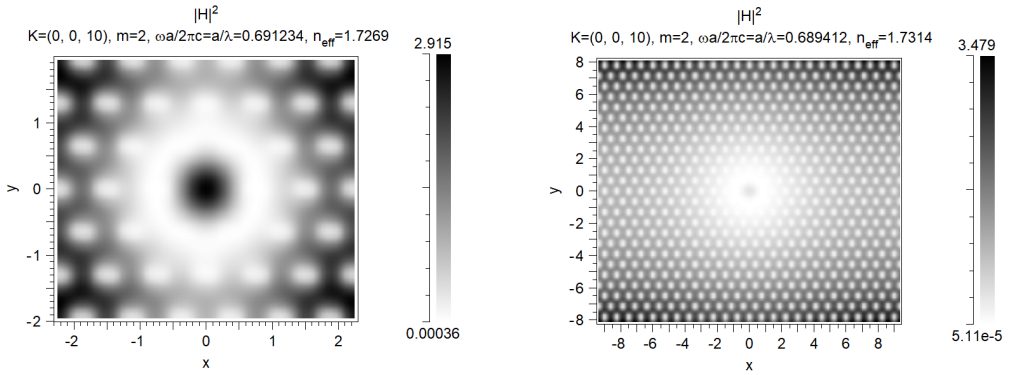

(a) Leaky mode

(b) Leaky mode in a bigger cell.

Figure 4.24: The same leaky mode but using different cell sizes.

Looking at these results, we could see that when the cell size is increased, the "leaky mode" disappears, and a minimum of intensity becomes visible where, previously, there was a maximum. See Figure (4.24b). The conclusion was that, this kind of profiles whether they are "leaky modes" or numerical remainders, are not confined

modes i.e. radiation modes. So, those waveguides that we thought that were not single-moded, we have demonstrated that, actually they are.

So, we came up with the hypothesis that Equation (4.3) was valid for conventional waveguides but can not be generalized for all PCWs. Furthermore, a 1.75 μm period is not a realistic number for a PCW because pores are too separated and light can sneak through the cladding between them. Also, when pores are too far away from each other, the core or cavity shape is not well defined as it can be seen in case **a.** of Figure (4.23). Thus, we concluded that, to look for the single-mode condition for MOWs, it is not recommendable to use V_{number} and, instead of that, we would analyze mode profiles.

Therefore, the intensity near-field mode profiles of waveguides with periods between 0.3 μm and 0.75 μm were studied. Also the pore width was changed to 200 nm and 400 nm for the analysis. The objective of doing this was to study the ratio between the width pore (d) and period (Λ) and their relationship with the number of propagation modes in the waveguide. From this study, we conclude the following points.

1. As we said before, a very large period is not feasible in a practical way because it leads to very long distances between the pores, which is not useful for light propagation. However, if we fix the ratio $\frac{d}{\Lambda}$ and the pore width and period are increased in such a way that the value of this ratio is maintained, it is possible to maintain the shape of the cavity and avoid leaks between the pores because pore widths have been increased and there is no dielectric cladding through which light can escape. The only significant dielectric region is the core. The important fact is that, in this case, cavity size is very large and a big number of modes can be guided in defect. If pore width and period are decreased in the same way, the core region will be small but still enough for guiding. The only change is that the number of confined modes in the waveguide is less than in a larger pore width and period PCW.

2. Also, pore width can be varied when period is fixed. Given a constant period, using different pore widths, it is possible to determine the ratio at which the leakages between pores occurs. This is almost the same that happens when the cladding lattice has very long periods. The space between pores is very large and, consequently, light can leak from the core and propagate through the periodic array of air holes, giving raise to radiation or "cladding" modes.

3. A similar result is obtained when the pore width is fixed and period increases its value. The reason is the same as in the previous paragraph because, when period is increased the space between pores becomes larger and radiation or cladding modes appear. This behavior is shown in Figure (4.25).

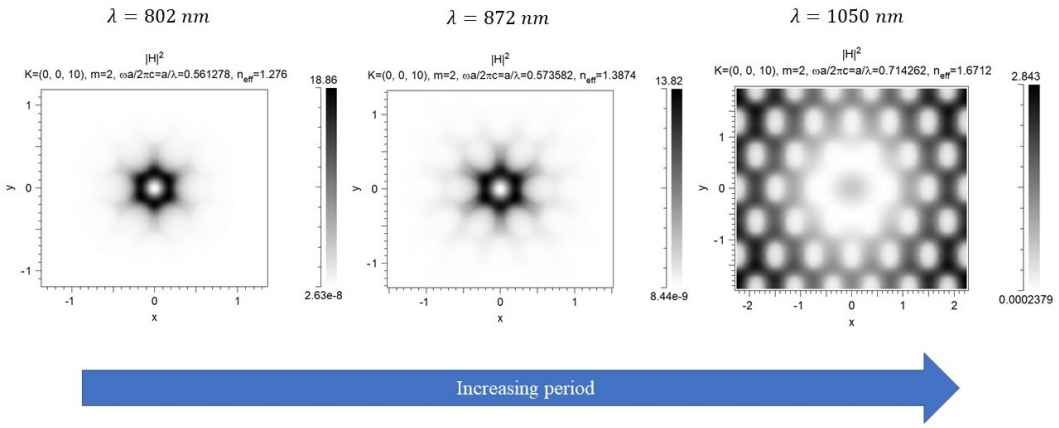

Figure 4.25: Example of higher order modes (HOM) for increasing lattice period.

Chapter 5

Conclusions.

En esta sección se recogen de manera resumida todas las conclusiones e interpretaciones obtenidas de los resultados. Se hace referencia tanto a los obtenidos experimentalmente como con el software de simulación.

In this project we have obtained relevant conclusions for both experimental and simulation results.

But first of all, we did a review about periodic structures and their characteristics. Also, we learned new concepts about photonic structures and increased our knowledge about Electromagnetism and Optics by studying the interaction of light with these devices.

Experimental results were, in general, satisfactory. The values of the measurements fell within the expected and could be explained by physical arguments. We were able to study the dependence between the longitudinal length of the pores and different parameters of fabrication. Also it was possible to confirm that, pore width and height decreased for decreasing power values. In some occasion, a few technical problems had be overcome before reaching to the final results. One example would be the delays caused by the SEGAI. Due to this, we also realized that experimental assignments require some conditions which, for many external facts, are not always available.

Simulation results also provided us interesting conclusions in order to apply them in a future laboratory work. We were able to study in a visual point of view the different modes of light propagation and an analysis of the single-mode condition was carried out. Needless to say that, to obtain these results, it was necessary to learn the use of ImageJ and BandSOLVE software and this information will be very useful for future applications. However, due to lack of time, it was not possible to recreate waveguide structures in the laboratory determining a starting point for future work.

Bibliography

[1] Von Freymann, G. and Linden, S (n.d.). *Photonic Crystals, Plasmonics and Metamaterials*[Lectures, Karlsruhe University]

[2] Maruo, S., Nakura, O and Kawata, S (1997). Three-dimensional microfabrication with two-photon polymerization*Opt. Lett*(22),132-134.

[3] Ródenas A., Gu M., Corrielli G, Paiè P., Sajeev J., Kar A.K. and Osellame R., (2018). Three-dimensional femtosecond laser nanolithography of crystals. *Nature Photonics*, (13), 105–109.

[4] Rumpf, R.C. [EMPossible]. (2020, May y 16). Lecture – Introduction to Periodic Structures [Video]. YouTube. *https://www.youtube.com/watch?v=utNLeRwqkQ8*

[5] Rumpf R.,(2020). *Introduction to Periodic Structures in Electromagnetics*[Lectures, University of Texas at El Paso]

[6] Rumpf R.,(2020). *Unit Cells and Brillouin Zones*[Lectures, University of Texas at El Paso]

[7] Rumpf R.,(2020). *Electromagnetic Waves in Periodic Structures*[Lectures, University of Texas at El Paso]

[8] National Institutes of Health. (1997). ImageJ (1.52p) [Software]. Recuperado de `https://imagej.nih.gov/ij/download.html`.

[9] Synopsys, (2020). RSoft. BandSOLVE User Guide, (v2019.09) .

[10] RefractiveIndex.INFO `https://refractiveindex.info/?shelf=main&book=Y3Al5O12&page=Zelmon`